Advanced Laboratory Course

– E213: Analysis of Z_0-decays –

Supervisors
David Hohn
Andrea Sciandra

Summer Term 2017

Abstract

The goal of this experiment is to understand the main ingredients of an analysis in particle physics. To understand how such an analysis is developed, we study data taken by the OPAL-experiment. In detail the decay of the heavy vector boson Z^0 will be examined during the experiment. Therefore a set of selection criteria for the dominant decay modes will contrived from single events of the detector. These criteria are then refined using Monte-Carlo-simulations of the decay modes with a higher statistic. On the basis of this one can deduce the efficiency from Monte-Carlo-simulations. With this fine-tuned selection various properties of the Z^0-boson can be determined.

Contents

1 Introduction

In particle physics the fundamental description of all processes can be deducted from the standard model of particle physics. It describes the three forces, namingly the strong, electromagnetic and the weak force, and the twelve elementary fermions of which all matter is built up. In 2012 the main missing ingredient, the HIGGS-boson, was found, such that the standard model is now tested to high precision. At the beginning of this model one of the most important predictions was the existence of the two heavy vector bosons that mediate the weak force, the Z^0 and the $W^{\pm}$. The search for those two bosons was mainly performed at the Large-Electron-Positron-Collider (abbreviated: LEP) at CERN. In this experiment the focus lies on the OPAL-experiment, which will be discussed in detail in the following section.

1.1 The OPAL-experiment

The OPAL-experiment was set up in the 1980s and 1990s to search for the Z^0. It is a typical collider experiment meaning that it has a rotational symmetry around the beam-axis. A sketch of the experiment is given in fig. 1.

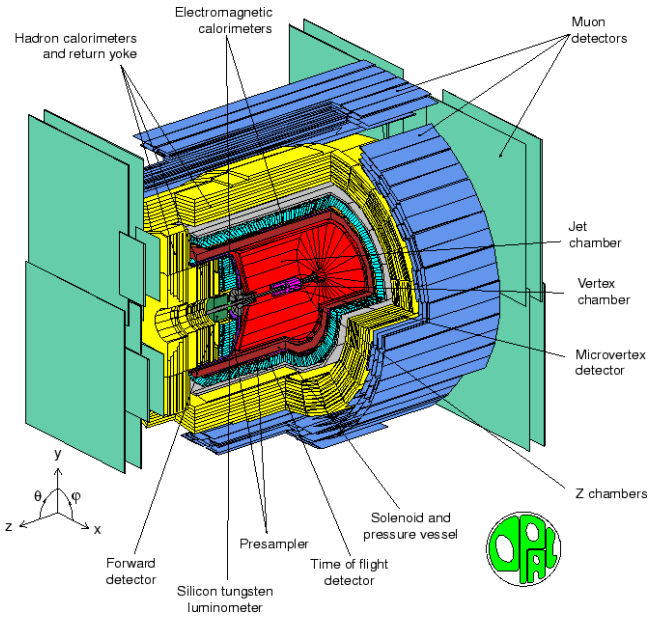

Figure 1: Sketch of the OPAL-experiment (exploded view, taken from [UCL])

In the center of the detector the beams collide, such that the final state particles emerge from this point. Nearest to the beam pipe a vertex tracker is mounted, which is able to measure the so called track of charged particles. In addition a magnetic field along the beam pipe causes the tracks to bend. From the curvature of the tracks one can deduce the momentum of the particle and the charge. In fig. 1 this component is shown in red. During the analysis this detector component will provide two observables. The first one is the number of charged tracks measured and the second one is the scalar sum of the momenta.

In the following sections we will discuss expectations on these variables for different channels taken into account in this analysis.
Further away from the beam-pipe the electromagnetic-calorimeter, which measures the energy of the electrons, positrons and photons that are present in the reaction. This is done via the bremsstrahlung, where an electron looses energy by emitting a photon, and the pair production, which describes the conversion of a photon into an electron-positron-pair. Of course the outgoing particles of both these reactions will undergo the same processes until nearly all the energy of the incidental particle is deposited within the calorimeter. Also heavier particles, mostly hadrons, will loose some energy in this calorimeter but they will probably surpass and leave the detector system. This process is then called the electromagnetic shower. For the analysis the sum of all energy depositions in this detector will be available.
The second most outer detector system of the setup is the hadronic calorimeter, which measures the energy deposition of the produced mesons and baryons. Similar to the electrons and photons in the electromagnetic calorimeter hadrons will produce a hadronic shower in this calorimeter, however the underlying processes are not as easy to describe. Again the sum of all energies will be available in the analysis of events. In comparison to the electromagnetic calorimeter the hadronic one has a much higher density to heighten the interaction probability for the hadrons. It is shown in yellow.
All we are left with are the muon shields in the most forward direction and on the outer boundaries of the detector. As the name proposes this component will measure the energy deposition of muons. At this point one can be sure that only muons reach it since the rest will have interacted in one of the other components. The muon shield is shown in fig. 1 in blue and turquoise. For reasons unknown to us the measurements of this system will be unavailable for the main part of the experiment.

2 Predictions and theory

As mentioned in the introduction the main task of this experiment is the analysis of the properties of the Z^0 and its decays. In particle physics the main properties of a particle are its mass, its width and the partial width into the allowed decay channels. In this chapter we will introduce these parameters along with theory calculations.

2.1 Mass and width of a resonance particle

In particle physics mass or also invariant mass just describes the physical LORENTZ-invariant mass of a given particle. The width however is only defined for particles that can be produced as a resonance in an interaction and then decay into further particles. Since the distribution of the events of the decays w.r.t. the energy reminds of the properties of a driven oscillator the width is defined analogously. The shape of the so called BREIT-WIGNER-distribution is shown in

fig. 2, where the width is denoted as Γ being the full width at half maximum of the distribution.

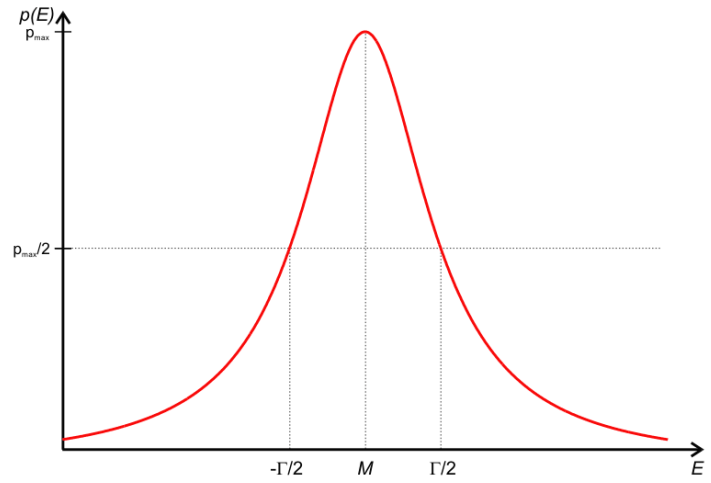

Figure 2: Example for a BREIT-WIGNER-distribution (taken from [WiBW])

The cross section of each decay channel of the Z^0 has a BW-shape and can be parametrized as given in the equation below.[1] Here the center of mass energy that is available at each point is given as s. The constants appearing here are the total decay width Γ_{Z_0}, the partial decay width into e^+e^- as Γ_e and the partial decay width into the fermion-antifermion pair of the decay channel Γ_f.

$$\sigma(s) = \frac{12\pi\hbar^2 c^2}{M_{Z_0}^2} \frac{\Gamma_e \Gamma_f \cdot s}{(s - M_{Z_0})^2 + \left(\frac{s^2 \Gamma_{Z_0}}{M_{Z_0}}\right)^2} \tag{1}$$

It has been mentioned that the Z^0 allows different decay channels, those are the decay into a pair of two oppositely charged leptons (denoted as the ee, $\mu\mu$, and $\tau\tau$- channels), two oppositely charged up-type or down-type quarks (all summed up as the $q\bar{q}$-channel). Several of these channels can be described in common since the decay only depends on the quantum numbers which do not change with the particle generation in the standard model. Another decay that was not mentioned before is the decay into two uncharged neutrinos, since it is not measurable directly with modern methods due to the nature of neutrinos. However the partial width of each of these channels is a measure for the probability of a Z^0 to decay in this channel. From the standard model one can derive that the partial width can be calculated from eq. 2.

$$\Gamma_f = \frac{N_c^f \cdot \sqrt{2}}{12\pi} G_F \cdot M_Z^3 \cdot \left(g_{V,f}^2 + g_{A,f}^2\right) \tag{2}$$

Here $g_{V,f}^2$ and $g_{A,f}^2$ are just constants one can easily calculate from the quantum numbers and the WEINBERG-angle, which was introduced to the standard model in the electroweak unification which would exceed the scope of this report. With this formula one can then calculate the partial widths of the different decay

[1] Any equations and numbers without further reference are taken from [E213].

channels, the results are shown in tab. 1. Comparing these results to the

channel	g_V	g_A	N_c	Γ_{partial} [GeV]	Γ_{sum} [GeV]	σ_{peak} [GeV^{-2}]	Δ [%]
e, μ, τ	-0.038	-0.5	1	0.083	0.250	$4.30{\cdot}10^{-6}$	3.08
ν	0.500	0.5	1	0.166	0.498	$8.56{\cdot}10^{-6}$	6.13
u, c	0.192	0.5	3	0.285	0.856	$1.47{\cdot}10^{-5}$	10.54
d, s, b	-0.346	-0.5	3	0.368	1.103	$1.90{\cdot}10^{-5}$	13.59
total					2.707	$4.66{\cdot}10^{-5}$	

Table 1: Theoretically predicted widths and cross sections of the Z^0 for different channels. Δ describes the relative difference of Γ_{Z_0} if there was another particle of this channel.

widths given in [PDG-Z] yields that only the width Γ_e and the width Γ_ν lie in good accordance with the latest measurements. For example the width of the Z^0 decaying into neutrinos is given as (503 ± 16) MeV which is compatible with the theoretical prediction by us which is 498 MeV. One can easily explain the deviations seen, for example we found Γ_q as 1.959 GeV while the latest measurements yield a value of (1744.0 ± 2.0) MeV, knowing that the formula we used neglects the masses of the particles. Therefore the phase space for the reaction is overestimated and the widths end up to be expected too large. However the deviations are negligible for the leptons and the neutrinos since the leptons are nearly massless compared to the Z^0 and the standard model data so far is compatible with massless neutrinos all along.
Accordingly also the peak cross-sections in the channels and the total width are reproduced with the same deviations. However one can calculate the relative change in the width of the Z^0 if another generation of one of the particles would exist below the mass of the boson. Since the percentages, as we will see later, are out of the range of the experimental uncertainty this predicts that there is no further particle generation. Nevertheless there could be other non-interacting particles beyond the standard model, which are the scope of current researches all over the world and will not be discussed here.

2.2 Cross sections

The cross section has been mentioned several times before. It is a measure for the probability of an interaction. Is has the dimension of an area due to its origin in mechanics. The scattering of a particle off of a sphere can be fully described knowing which physical (macroscopic) cross section the sphere has. In particle physics and optics however the cross section holds no implications on the physical size of the scattering center. From an experimentalists view the cross section is not more than the ratio of incoming particles per target area and the outgoing decay particles. The observable for the total amount of incoming particles in a collider experiment is the integrated luminosity $\int \mathcal{L} dt$, while the total amount of outgoing particles is to be determined in the experiment. For the definition of the cross section it is assumed the number of outgoing particles is N_{out}. Then the cross section is defined to be the proportionality constant as

$$N_{\text{out}} = \sigma \cdot \int \mathcal{L} \mathrm{d}t \,. \tag{3}$$

2.3 Angular distributions and asymmetry

In the case that two outgoing leptons are observed, we define the scattering angle as the angle between the incoming electron and the outgoing negatively charged lepton. In this section we will only discuss the ee- and $\mu\mu$-channel since such an angle can only be defined for exactly two outgoing particles. The other channels will not have two outgoing charged particles since the τ-leptons decay before leaving the beampipe and the quarks hadronize immediately since quarks can not exist as single particles.

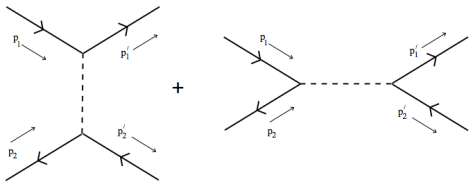

Figure 3: Visualization of the s- and t-channel

The process we are investigating completely takes place in the so called s-channel, which means that the incoming particles annihilate into a resonance particle which then decays. This can be visualized in a diagrammatic fashion as seen in fig. 3 on the right side. The differential cross section w.r.t the decay angle of such processes obeys an angular distribution proportional to $\left(1+\cos^2\theta\right)$, which can be seen as the green curve in fig. 4.

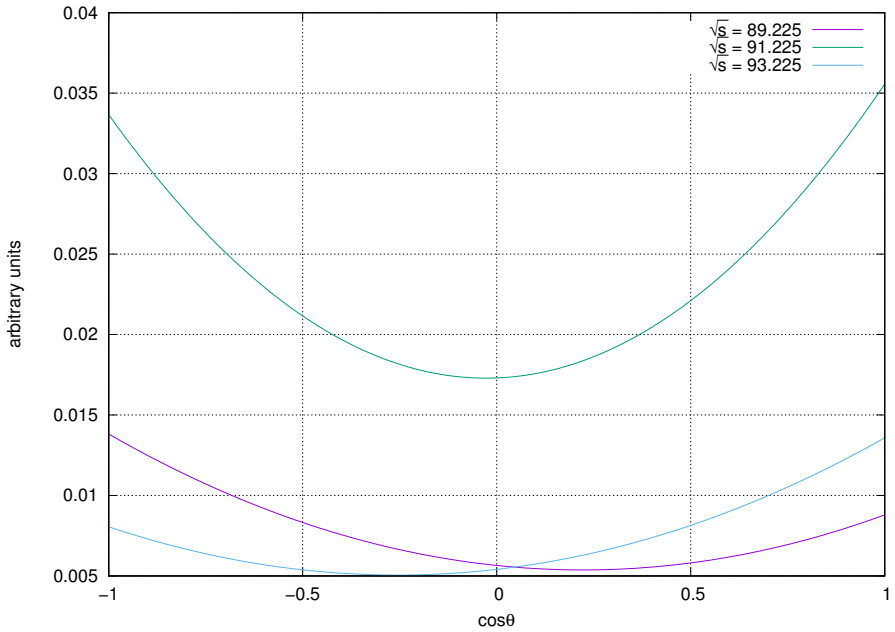

Figure 4: Angular distribution of $ee \to \mu\mu \backslash ee$ in s-channel at different energies.

For the ee-channel also the t-channel interaction is allowed since the incoming and outgoing particles can be identical. This type of interaction is also shown

as a diagram on the left side of fig. 3. Here the cross section is proportional to $(1-\cos\theta)^{-2}$ as shown in fig. 5. This distribution of the t-channel events is accordingly dominated by those with a small scattering angle. Accordingly they can be cut from the data set using this variable. Another useful outcome of this distribution of the so called BHABHA-scattering of e^+e^- is the integrated luminosity, since the theory for this scattering is so well understood that it can be used to fix this observable. Therefore only events that happen to have outgoing electron-positron-pairs in the most forward direction are taken into account. The number of those is then divided by the cross section to achieve the integrated luminosity.

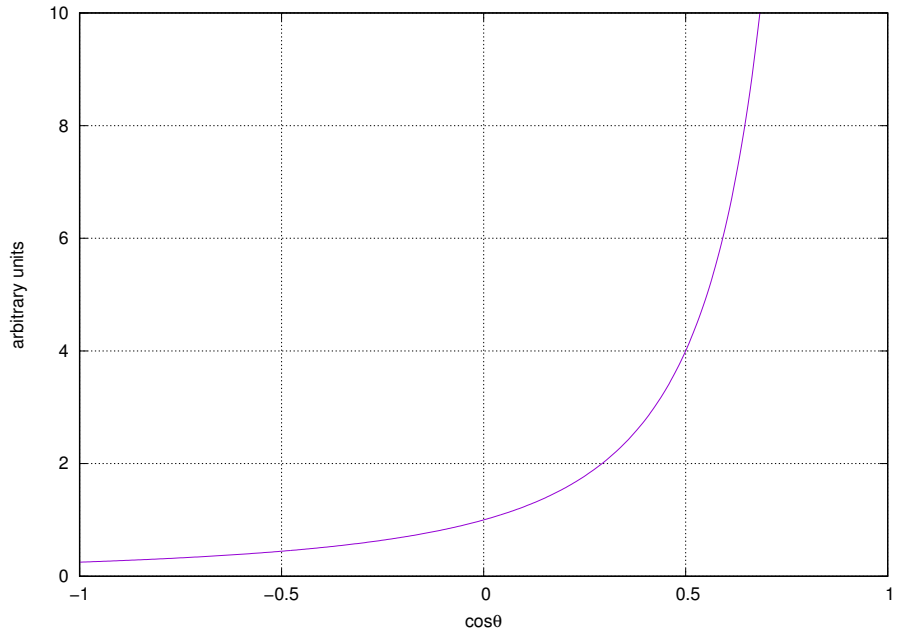

Figure 5: Angular distribution of $ee \to ee$ in t-channel near the Z^0-resonance.

2.3.1 Forward-Backward-Asymmetry

In the BORN-approximation the differential cross section for the process $ee \to f\bar{f}$ reads:

$$\frac{\mathrm{d}\sigma}{\mathrm{d}\Omega} = \frac{\alpha^2 N_c^f}{4s}\left[F_1(s)\left(1+\cos^2\theta\right) + 2F_2(s)\cos\theta\right] \tag{4}$$

with

$$F_1(s) = Q_f^2 - 2v_e v_f Q_f \,\mathrm{Re}(\chi) + \left(v_e^2+a_e^2\right)\left(v_f^2+a_f^2\right)|\chi|^2 \tag{5}$$

$$F_2(s) = -2a_e a_f Q_f \,\mathrm{Re}(\chi) + 4v_e a_e v_f a_f \,|\chi|^2 \tag{6}$$

where Q is the electric charge and v and a are the vector- and axialvector coupling strengths of the fermion. Those values have already been given in tab. 1. χ however is the so called propagator. From the form of the diff. cross section one can directly see that it is not manifestly symmetric in the angle θ, therefore

this leads to an asymmetry in the data. First of all we define the integral

$$\mathcal{I}(x,y) = \int_x^y \frac{\mathrm{d}\sigma}{\mathrm{d}\cos\theta}\mathrm{d}\cos\theta \tag{7}$$

With this the forward-backward-asymmetry can be written as:

$$A_{FB} = \frac{\mathcal{I}(0,1) - \mathcal{I}(-1,0)}{\mathcal{I}(0,1) + \mathcal{I}(-1,0)} = \frac{3}{4} \cdot \frac{F_2}{F_1} \tag{8}$$

This can be used to measure the WEINBERG-angle θ_W that has already been mentioned, since the coupling strengths are proportional to it. The WEINBERG-angle comes to existence from the mixing of the Z^0 and the photon in the electroweak interaction, which is the unification of electromagnetism and the weak force. Any further description of the unification would exceed the scope of this report, but we can use the measurement of the asymmetry to determine the $\sin^2\theta_W$, which is an important constant in the standard model. According to the predictions from the theory given in equation 8 one can calculate predictions for the asymmetry at different center-of-mass energies in dependence of the WEINBERG-angle. The obtained predictions are given in tab. 2, later on we will than be able to use these predictions to rule out which of the angles gives the correct results.

$\sin^2\theta_W$	$\sqrt{s}$ [GeV]	Re(χ)	$\lvert\chi\rvert^2$	F_1	F_2	A_{fb}
0.21	89.225	-15.571	351.105	51.330	-10.605	-0.155
0.21	91.225	1.068	1133.380	163.687	4.443	0.020
0.21	93.225	15.703	362.243	53.062	12.995	0.184
0.23	89.225	-15.571	351.105	45.162	-10.001	-0.166
0.23	91.225	1.068	1133.380	143.761	3.947	0.021
0.23	93.225	15.703	362.243	46.690	12.104	0.194
0.25	89.225	-15.571	351.105	40.395	-9.498	-0.176
0.25	91.225	1.068	1133.380	128.363	3.561	0.021
0.25	93.225	15.703	362.243	41.765	11.379	0.204

Table 2: Theoretically predicted forward-backward-asymmetry and most important intermediate steps in the calculation for different WEINBERG angles and different energies.

2.4 Radiative corrections

Everything that was taken into account so far were so called tree-level diagrams, which means only two interaction vertices are allowed with one vector boson. However it is also possible that one of the initial state particles emits a photon and thereby looses energy. This effects will deform the cross section as shown in fig. 6.

Hence the radiative corrections shift the maximum of the distribution slightly to higher s and gives a rise to events on this site. This behaviour is well understood, because if the center-of-mass energy in the beginning was higher than the resonance energy it can be quite well shifted nearer to the maximum by the emission of a photon. And since the photon can have an arbitrary energy this

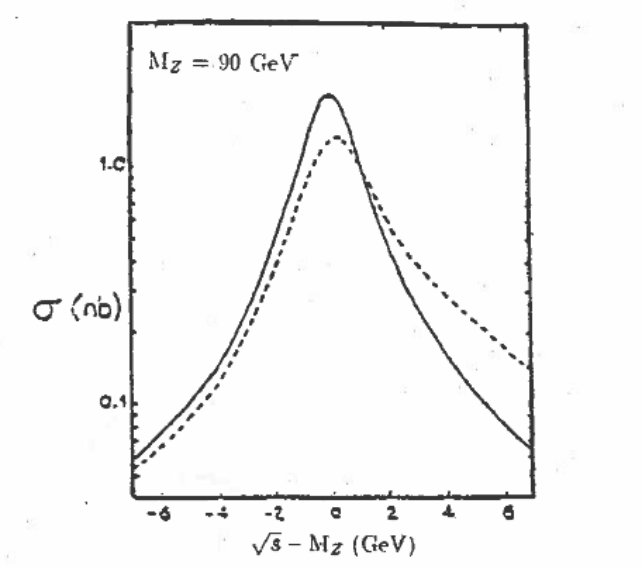

Figure 6: Cross section of the Z^0-production without (solid) and with radiative corrections (dotted) taken form [E213]

effect can extend to arbitrary high s, but it gets more unlikely with higher s. In this report we will just add corrections as constant summands to our cross section to cope with this effect. Those constants have been determined earlier and are given in [E213].

3 Development of selection criteria

In the previous sections we discussed the main parts of the detector system and the physics we want to investigate. In this section we will discuss how we developed a selection for events from the Z^0-decay.

3.1 Graphical analysis of the different channels

On the first day of the experiment we started looking at events for the different channels with `GroPE`, which is a tool developed for the needs of this experiment. `GroPE` can visualize events from the detector system showing the different components. Thus we could get a feeling what a typical event in each channel looks like.

3.1.1 Visualization of the *ee*-channel

From the theory one expects the decay of the Z^0 into an electron-positron-pair to end with two high energetic electrons in the final state. From the properties of the detector components one can then deduce that such processes cause two charged tracks in the tracking system that carry the complete energy of the decay, hence the `SUMP` is nearly the center of mass energy. The to e-like particles will then depose all their energy in the electromagnetic calorimeter, while the other components should not show any signals. A typical event from this channel is shown in fig. 7. Here one can clearly see the two prominent charged tracks (blue) and their energy deposition in the electro magnetic calorimeter (yellow). Another constraint from the nature of this decay being that the two particles have to go exactly in opposite directions can be seen in fig. 7 and also stays true when looking at the event in sideview (see fig. 8). It is also obvious that neither the hadronic calorimeter nor the muon chambers have measured a signal in this event.

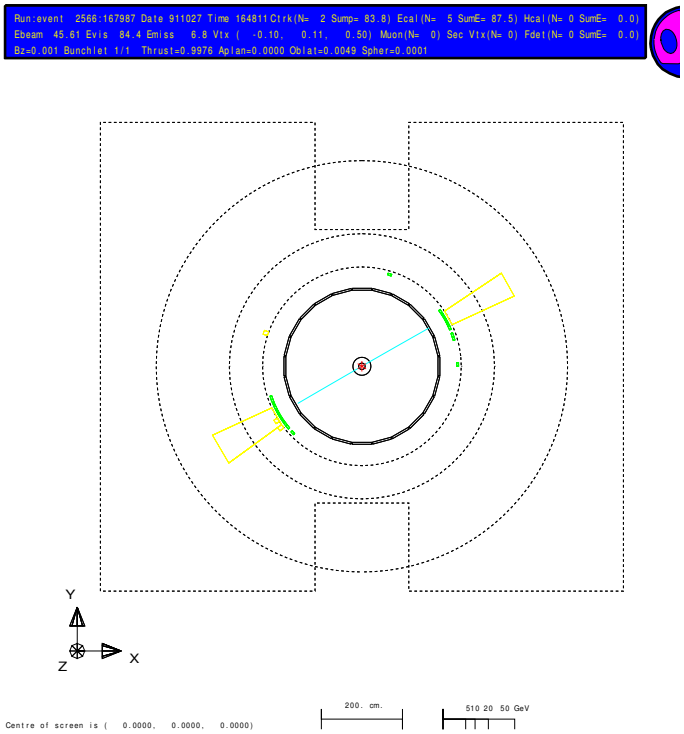

Figure 7: A typical event from the ee-channel in xy-view

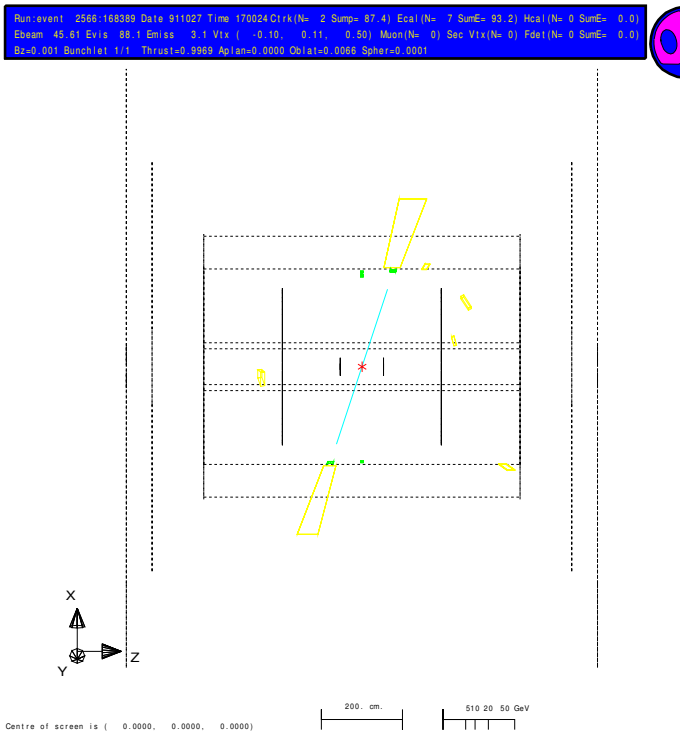

Figure 8: A typical event for the ee-channel in xz-view

3.1.2 Visualization of the $\mu\mu$-channel

As in the ee-channel also the $\mu\mu$-channel has two high energetic charged leptons in the final state, hence also two charged tracks that are exactly opposite to each other are expected in this channel. In contrast to electrons muons loose nearly no energy in the calorimeters but will leave a signal in the muon chambers. These properties of the $\mu\mu$-channel can clearly be seen in fig. 9. Again the tracks are shown in blue and the electromagnetic calorimeter hits in yellow. The hadronic calorimeter hits can be seen in pink and the hits (with direction) in the muon chambers are pictured as arrows. Again the sideview confirms that the two muons go into exactly opposite directions (see fig. 10).

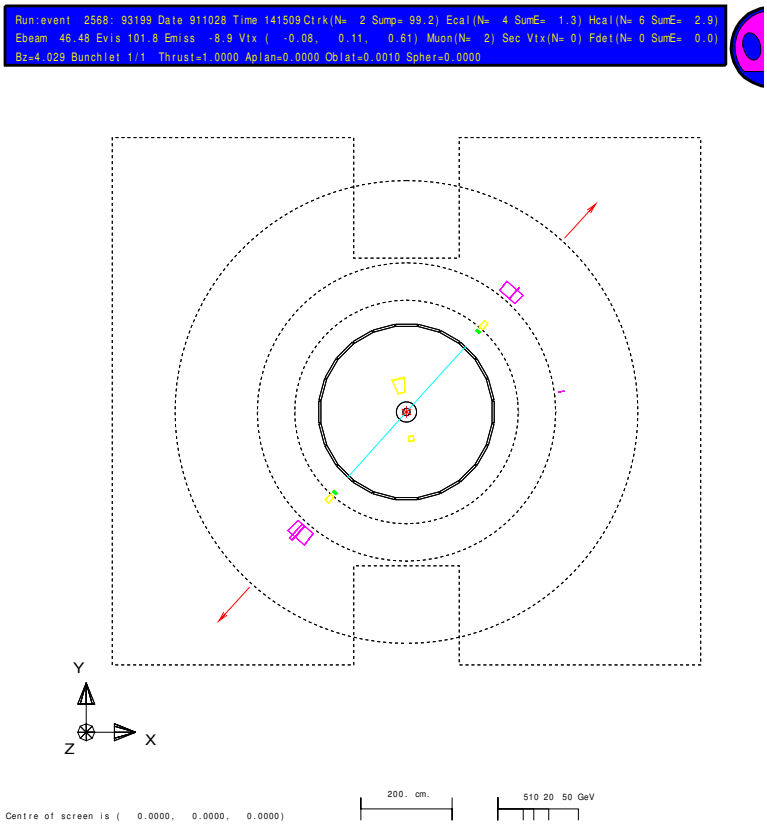

Figure 9: A typical event from the $\mu\mu$-channel in xy-view

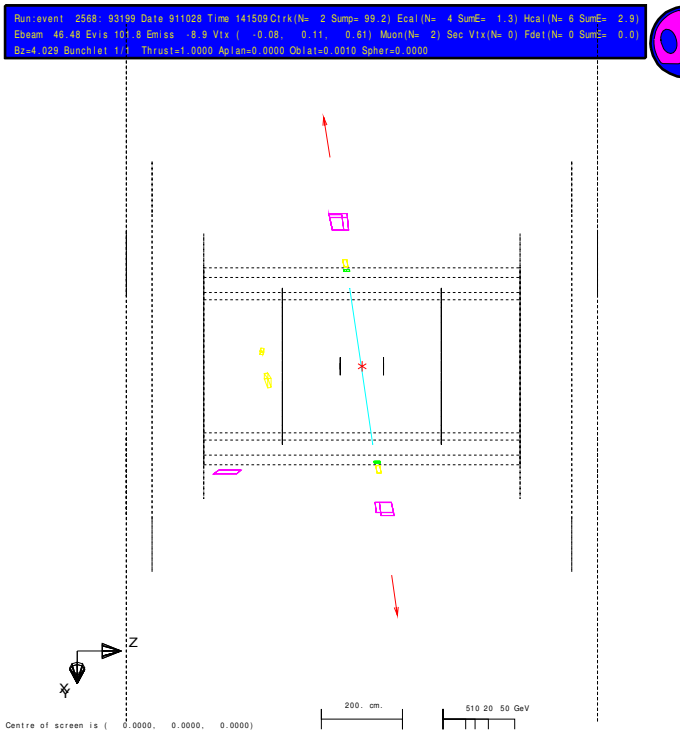

Figure 10: A typical event from the $\mu\mu$-channel in xz-view

3.1.3 Visualization of the $\tau\tau$-channel

In contrast to the other leptonic channels the $\tau\tau$-channel does not necessary have two charged particles in the final state, since the τ decays. Hence it is expected that the number of charged tracks is higher in this channel. However one expects to have two independent clusters of charged tracks in opposite directions, since each τ decays individually. Depending on the decay products, which are mainly muons and pions along with at least one τ-neutrino to conserve the lepton number, there will be energy depositions in the detector systems. One can distinguish the different decay modes of the τ-leptons by the number of charged tracks which are then called *prongs*. As an example for the $\tau\tau$-channel the event in fig. 11 was chosen, it shows a 4-prong event. The four charged tracks that can be seen in the figure (blue) belong to three charged pions and a muon emerging from the incidental τ-leptons. As described before the muon on the one side does not depose much energy in the electromagnetic and hadronic calorimeter but can be seen in the muon chamber. On the other side the three charged pions loose some of their energy in the electromagnetic calorimeter and then depose the remaining energy in the hadronic calorimeter (pink). Since the 4-prong event is only one possible final state of the decays of the τ-leptons there can not be made more statements on the general properties of this channel.

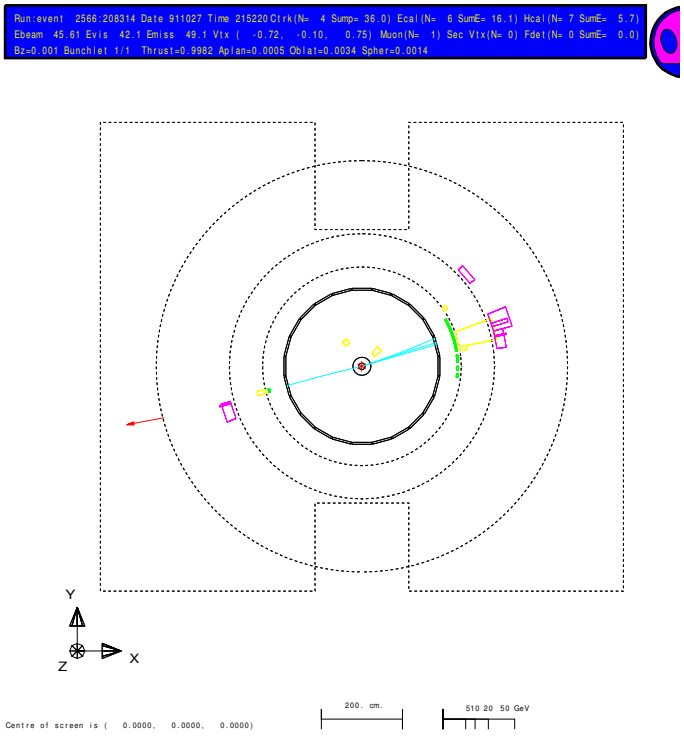

Figure 11: Typical 4-prong event from the $\tau\tau$-channel

3.1.4 Visualization of the $q\bar{q}$-channel

Since quarks can not exist as free particles due to their colour charge, the two quarks from the decay will instantly hadronize. That means that extra $q\bar{q}$-pairs are created from the vacuum so that these can form bound states. This process will, as the theory predicts, lead to two so called jets, which are bigger clusters of charged tracks. Depending on the particles produced in the jet there can be signals in all detector components. For example charged pions lead to signals in the electromagnetic and hadronic calorimeter. If they decay before reaching the calorimeters also muons from their decay can reach the muon chambers. The most general observation of this channel is that it has a large number of charged tracks. A typical event for the $q\bar{q}$-channel can be seen in fig. 12. Here it is obvious that all detector components probably will measure a particle in such a decay, while the sum of the momenta in the tracker is not necessarily in the range of the center-of-mass energy since neutrinos can take away a certain amount of the momentum.

3.2 First determination of selection criteria

`GroPE` also makes the already mentioned variables `E_ECAL`, `E_HCAL`, `SUMP` and `NTRK` available for the user. With this we looked at 20 events for each channel and histogramed the 4 variables. The tables with the data can be found in the appendix. Since the information about the muon chambers is not available later we did not take these into account here. From the histograms we then deduced a decision tree to determine the nature of the event. Here we imposed independ-

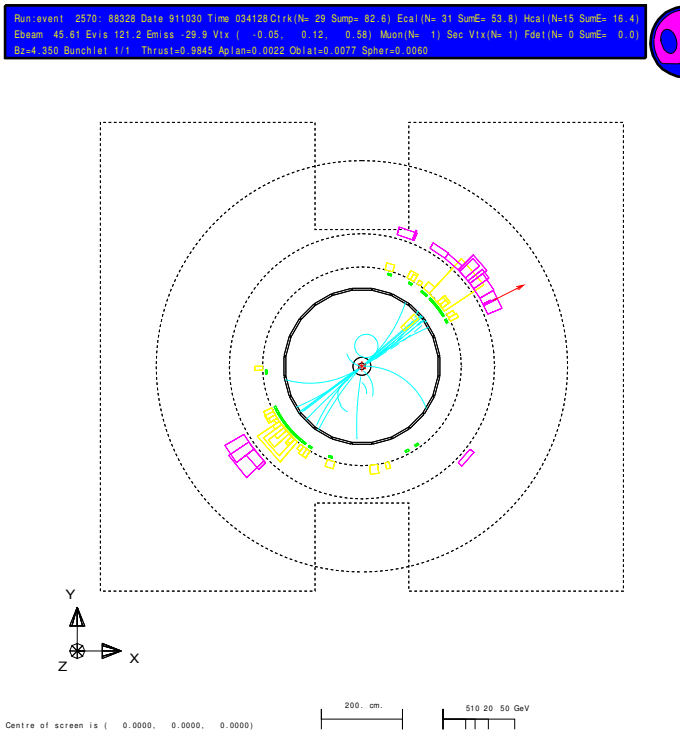

Figure 12: A typical event in the $q\bar{q}$-channel

ent cuts on all variables, which means that we did not fix the borders of one cut to the value of another variable. As an example the number of charged tracks will be discussed, the according histogram is shown in fig. 13. It is obvious that this variable gives a handle on differentiating between leptonic and hadronic final states. This can be achieved by requiring at least 8 charged tracks for a hadronic event and at most 6 for a leptonic event. This cut is on the basis of the data given here without any loss of events and completely orthogonal. Here orthogonal means that there is no overlap of the two cutting regions.

To further distinguish between the ee and the other two leptonic channels the `E_ECAL`-variable can be used, since electrons will depose all their energy in this calorimeter. On the other hand muons will not loose much energy in this detector system and in the case of the τ-leptons there are at least two neutrinos that take away energy from the system. Hence we used the cutting conditions that `E_ECAL` $> 80\,\mathrm{GeV}$ for electrons and `E_ECAL` $< 60\,\mathrm{GeV}$ for the other two channels. The according histogram is shown in the appendix.

By now the $q\bar{q}$ and the ee-channels can be distinguished from each other and the other two leptonic channels, thus it is important to impose a cut to distinguish muons and taus. As already mentioned in the $\tau\tau$-channel there are at least two neutrinos that take away energy and momentum from the reaction. Hence the scalar sum of the momenta can be used to differentiate the channels with the cut `SUMP` $> 80\,\mathrm{GeV}$ for muons and `SUMP` $< 60\,\mathrm{GeV}$ for taus. The histograms for this variable can also be found in the appendix.

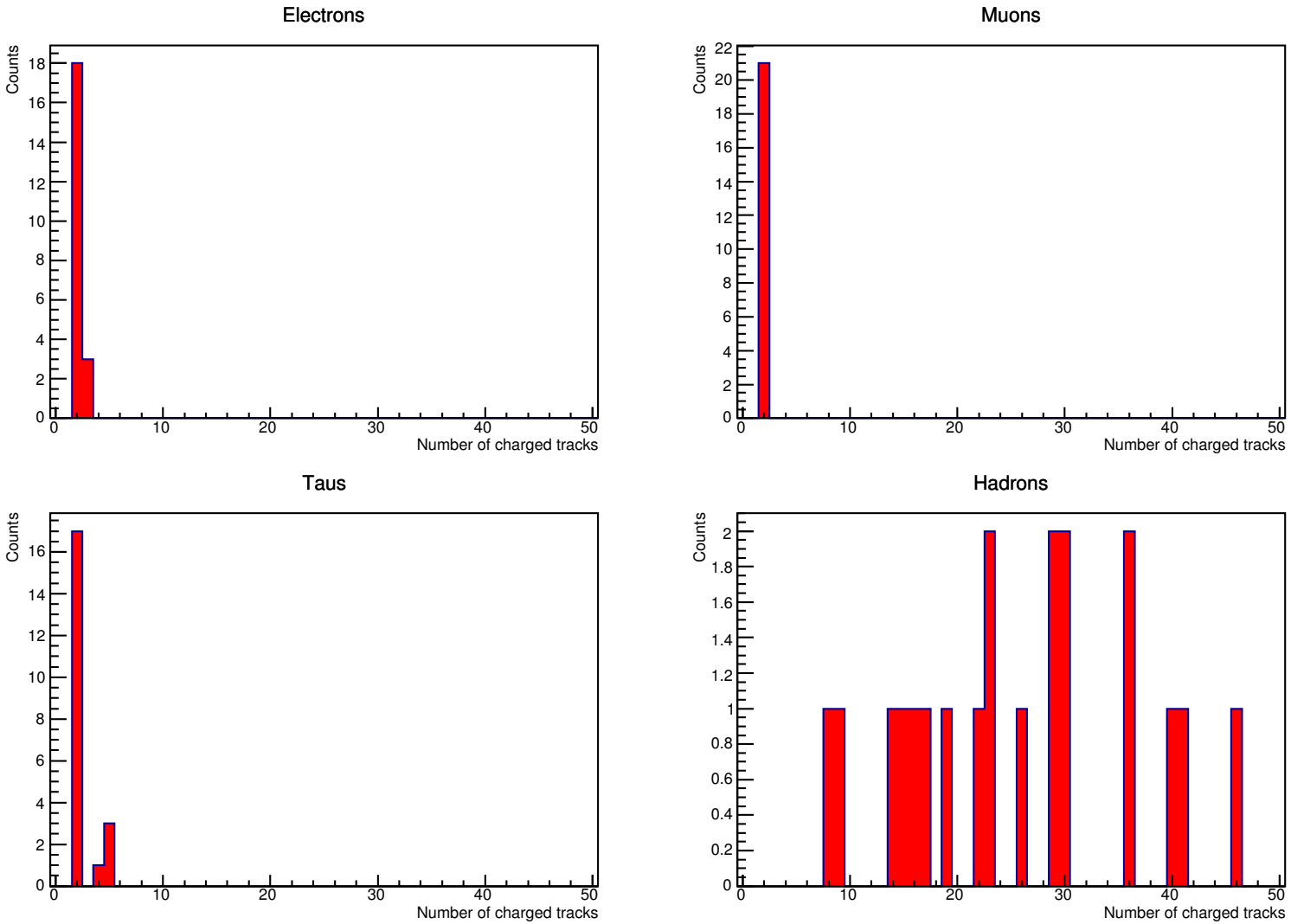

Figure 13: Histogram of the number of charged tracks for the different channels

With this cut we are able to distinguish the channels from each other. Later also a cut on the hadronic calorimeter was imposed also it was not needed in the first place. The used cuts are summed up in tab. 3, where the complete cut for each channel is the logic and of all independent cuts.

variable	$q\bar{q}$	ee	$\mu\mu$	$\tau\tau$
NTRK	≥ 8	≤ 6		
E_ECAL		$\geq 80\,\text{GeV}$	$\leq 60\,\text{GeV}$	
SUMP			$\geq 80\,\text{GeV}$	$\leq 60\,\text{GeV}$
E_HCAL	$\leq 30\,\text{GeV}$	$\leq 1\,\text{GeV}$	$\leq 30\,\text{GeV}$	

Table 3: Cuts determined using the GroPE-software

3.2.1 Test of the selection

After this development with pure data sets for each channel, the cuts were tested using a data set with mixed channels. During this test we could confirm that the cuts reproduce the same result as an optical analysis of the events. Hence the above cuts can be seen as a good estimation that has to be refined with higher statistics. Only one event in the test set was not determined well. This event can be seen in fig. 14. From an optical evaluation of the figure one would

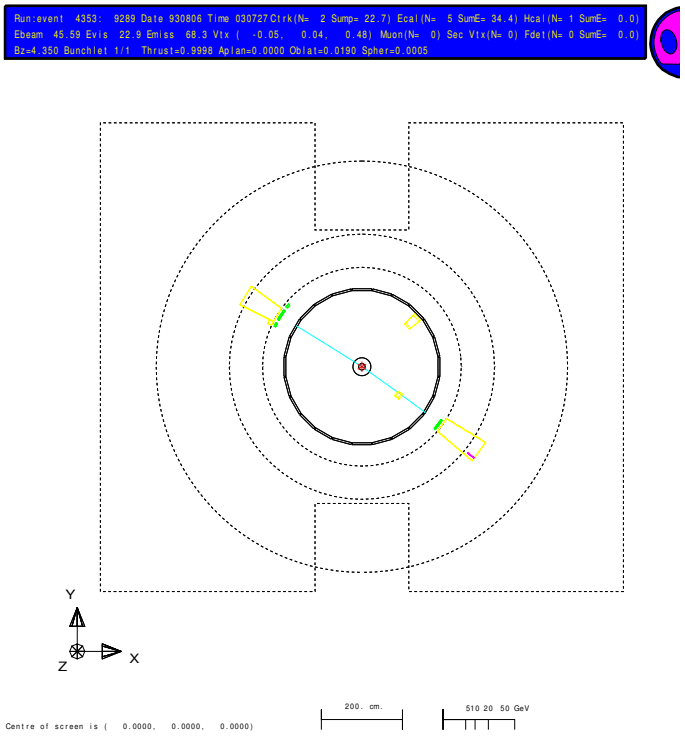

Figure 14: Event that would have been classified as $\tau\tau$ by the cuts explained above but does not belong in any category of interest, as it was not produced by a Z^0-resonance.

conclude that this event is clearly an ee-channel event, however the criteria given above would identify this event as a $\tau\tau$-event. We came to the conclusion that this event actually comes from a pair-production from a photon that was

emitted by an initial state particle that did not further interact. With the given variables there was no possibility to refine the cuts such that this event will not be counted as a $\tau\tau$-event. Given the rather small probability for such an event to happen, we did not further investigate it.

3.3 Refining of the selection criteria

As mentioned before the selection criteria above were developed using rather small statistics. In order to refine the cuts MONTE-CARLO-simulations were used. MONTE-CARLO-simulations are here used to simulate the scattering of the fermion-antifermion-pair in the final state and the interaction of those with the detector system. The simulations will also end in data files that are digitalized in the same way as in the original experiment, hence one can study deviations from the expectations on the data. The most important variable will be the selection efficiency, which will be discussed in detail in the next section.
First of all one can refine the cut criteria in such a way that as few as possible events are lost or missidentified. In the case of real data or MONTE-CARLO-simulations for the moment the distributions of the variables are broader and have more overlap between the event categories.
The first change in the cuts had to be done because in real events it can happen that the momentum can not be determined. This will lead to arbitrarily high unphysical momenta and is the case when the tracks have almost no curvature and are close to $\theta = 0$, because then the calculations are not numerically stable. Hence an upper limit on the `SUMP` of 200 GeV was introduced for all channels. This needs to be done because a differentiation between the different channels is impossible if the variable is not determined, since the other variables can not be trusted either then.
Another change of the cuts that had to be put in is that the upper limit of the `E_ECAL` was set to 20 GeV for muonic events, to lower the overlap to the $\tau\tau$-channel.
In the end the used cut regions can be summed up in tab. 4. During this analysis

variable	$q\bar{q}$	ee	$\mu\mu$	$\tau\tau$
`NTRK`	> 8	≤ 6		
`E_ECAL`		$\geq 80\,\text{GeV}$	$< 20\,\text{GeV}$	$< 70\,\text{GeV}$
`SUMP`	$[1\,\text{GeV}, 200\,\text{GeV}]$	$[1\,\text{GeV}, 200\,\text{GeV}]$	$[80\,\text{GeV}, 200\,\text{GeV}]$	$[1\,\text{GeV}, 60\,\text{GeV}]$
`E_HCAL`		$\leq 3\,\text{GeV}$	$\leq 30\,\text{GeV}$	

Table 4: Cuts determined with higher statistics using `PAW`

using `PAW`, which is a predecessor of `ROOT`, two other variables were introduced. Those were the scattering angle $\cos\theta$ and the thrust angle $\cos\theta_{\text{thrust}}$. The scattering angle is defined as described before, while the thrust angle is the angle between the incoming electron and the axis of maximal projection of the measured momenta. In this report the thrust angle was not needed for the calculations and could not be used for cuts reasonably. Nevertheless a cut on the scattering angle was introduced in the ee-channel to get rid of the t-channel events that are not coming from the decay of a Z^0. The used boundaries here

were $-0.85 < \cos\theta < 0.5$, where the lower boundary was chosen to also cut away events where the particles are too close to the beamline. This lower cut was used in order to make sure that the momentum could be consistently well determined as there can be unsecurities as explained above if the outgoing particles are too close to the beamline.

4 Analysis of the decay parameters

4.1 Normalization

In the case of the final state ee one has to remember that the scattering can take place over s-channel as well as t-channel. As we are interested only in the part of the cross section coming from the Z^0-resonance we have too add a cut in the scattering angle. The cross section of the t-channel is strongly peaked around $\cos\theta = 1$ and using only the data with $\cos\theta < 0.5$ leaves nearly only s-channel events. In addition there was made a cut $\cos\theta > -0.85$ because the detector cannot resolve the angle of this region properly.
For the efficiency calculations we want to normalize on the number of s-channel events N_s where the number of MONTE-CARLO-simulated events $N_{\text{mc}} = 100000$ is given and the rest N_t has to be t-channel events.

$$N_{\text{mc}} = N_s + N_t$$

Not every MONTE-CARLO-simulated event is detected and classified as ee but there is some preliminary efficiency ϵ_0 that can be calculated via the total number of measured ee-events $N_{\text{tot}} = \epsilon_0 N_{\text{mc}}$. In the end N_s has to be rescaled to the complete $\cos\theta$-interval by the factor

$$\epsilon_I = \frac{\int_{-1}^{1}(1+x^2)\text{dx}}{\int_{-0.85}^{0.5}(1+x^2)\text{dx}} \approx 1.67045$$

where $1+\cos^2\theta$ is the angular disribution of the s-channel. Putting this together with the number of events measured after all the cuts N_{meas} one gets

$$\begin{aligned} N_s &= \frac{\epsilon_I}{\epsilon_0} N_{\text{meas}} \\ &= 1.67045 \frac{N_{\text{mc}}}{N_{\text{tot}}} N_{\text{meas}} \\ &= 1.67045 \frac{100000}{93802} 19562 \\ &\approx 34836.5\,. \end{aligned}$$

For the other final states the efficiency can be calculated by normalizing with N_{mc}.

4.2 Efficiency

The efficiency is calculated as a matrix considering the four different final states. The matrix element

$$\epsilon_{ab} = \frac{N_{ab}}{N_a}$$

gives the probability of an event a being classified as an event b. Here N_{ab} is the number of events a classified as b and N_a is the total number of events a discussed in section 4.1. The different events are $a, b \in \{e, \mu, \tau, q\}$. The cuts were adjusted in a way to get as close as possible too $\epsilon_{ab} = \delta_{ab}$. The counts obtained by the MONTE-CARLO-simulations

$$(N_{ab}) = \begin{pmatrix} 18816 & 0 & 37 & 0 \\ 0 & 83048 & 74 & 0 \\ 243 & 1447 & 70954 & 454 \\ 1 & 0 & 241 & 96206 \end{pmatrix}$$

lead too the efficiency

$$(\epsilon_{ab}) = \begin{pmatrix} 0.540123 & 0 & 0.00037 & 0 \\ 0 & 0.83048 & 0.00074 & 0 \\ 0.00697544 & 0.01447 & 0.70954 & 0.00454 \\ 0.0000287055 & 0 & 0.00241 & 0.96206 \end{pmatrix}.$$

This allows us to calculate the measured number of events from the actual number of events. But for the evaluation of the data in order to obtain the cross sections one needs to calculate the number of actual events from the number of measured ones. This means that one has to invert[2] the matrix ϵ_{ab}.

$$\begin{aligned} \left(\epsilon^{-1}\right)_{ab} \quad = \quad & \begin{pmatrix} 1.85144 & 0.0000168225 & -0.000965496 & 4.55621 \cdot 10^{-6} \\ 0.0000162186 & 1.20414 & -0.00125587 & 5.92648 \cdot 10^{-6} \\ -0.0182017 & -0.0245573 & 1.40942 & -0.00665112 \\ -9.64656 \cdot 10^{-6} & 0.0000615165 & -0.00353063 & 1.03945 \end{pmatrix} \\ & \pm \begin{pmatrix} 0.00916288 & 6.00405 \cdot 10^{-6} & 0.000159176 & 4.64961 \cdot 10^{-6} \\ 0.0000151996 & 0.00174581 & 0.000144471 & 3.03009 \cdot 10^{-6} \\ 0.00116508 & 0.000661447 & 0.00287951 & 0.000322819 \\ 0.0000552868 & 5.37232 \cdot 10^{-6} & 0.000234855 & 0.000656034 \end{pmatrix} \end{aligned}$$

The error was computed using a MONTE-CARLO method. The matrix ϵ_{ab} is distributed according the binomial distribution

$$P(\epsilon_{ab}) \propto \epsilon_{ab}^{N_{ab}} (1 - \epsilon_{ab})^{N_a - N_{ab}}.$$

The error for the inverse matrix was now calculated by simulating ϵ_{ab} 1000 times from the binomial[3] distribution, inverting every matrix on its own and then calculating the standard deviation.

[2] All matrix calculations were performed by Mathematica.

[3] To reduce the numerical effort the binomial distribution was approximated by a normal distribution for large enough N_{ab} and by a linear function for $N_{ab} = 0$.

4.3 Cross sections

$\sqrt{s}$ [GeV]	$\mathcal{L}$dt [1/nb]	$\Delta\mathcal{L}$dt [1/nb]	correction$_{ll}$ [nb]	correction$_{\mathrm{qq}}$ [nb]
88.5	675.9	5.7	0.09	2.00
89.5	800.8	6.6	0.20	4.30
90.2	873.7	7.1	0.36	7.70
91.2	7893.5	54.3	0.52	10.80
92.0	825.3	6.9	0.22	4.70
93.0	624.6	5.5	-0.01	-0.20
93.7	942.2	7.7	-0.08	-1.60

Table 5: Luminosity used for data set six and radiation corrections for the total cross sections.

Using the cuts explained before for the real data[4] one gets the counts given in table 6 for the different energies and final states. These counts N_a are assumed to be normal distributed, thus having an error of $\sqrt{N}$. They have to be divided by the integrated luminosity from table 5 with the error

$$\begin{aligned} \sigma_a^0 &= \frac{N_a}{\mathcal{L}\mathrm{dt}} \\ \Delta\sigma_a^0 &= \sqrt{\frac{N_a}{(\mathcal{L}\mathrm{dt})^2} + \frac{(N_a \Delta\mathcal{L}\mathrm{dt})^2}{(\mathcal{L}\mathrm{dt})^4}}\,. \end{aligned}$$

Now every four-tuple $\sigma^0 = \left(\sigma_e^0, \sigma_\mu^0, \sigma_\tau^0, \sigma_q^0\right)$ of preliminary cross sections corresponding to one energy has to be multiplied from left by ϵ^{-1} in order to obtain the cross section σ corresponding too the Z^0-resonance in first order:

$$\begin{aligned} \sigma &= \epsilon^{-1} \cdot \sigma^0 \\ \Delta\sigma_a &= \sqrt{\sum_b \left(\left(\epsilon^{-1}\right)_{ab} \Delta\sigma_b^0\right)^2 + \sum_b \left(\left(\Delta\epsilon^{-1}\right)_{ab} \sigma_b^0\right)^2} \end{aligned}$$

In the end we add the leptonic and hadronic radiation corrections listed in table 5 receive the corrected cross sections in table 6.

[4] Data set number six.

$\sqrt{s}$ [GeV]	counts$_{ee}$	counts$_{\mu\mu}$	counts$_{\tau\tau}$	counts$_{qq}$	σ_{ee} [nb]	$\sigma_{\mu\mu}$ [nb]	$\sigma_{\tau\tau}$ [nb]	σ_{qq} [nb]	$\Delta\sigma_{ee}$ [nb]	$\Delta\sigma_{\mu\mu}$ [nb]	$\Delta\sigma_{\tau\tau}$ [nb]	$\Delta\sigma_{qq}$ [nb]
88.5	122	127	180	3483	0.42	0.32	0.42	7.36	0.04	0.02	0.03	0.10
89.5	291	341	355	7789	0.87	0.71	0.74	14.41	0.04	0.02	0.03	0.15
90.2	462	648	628	15400	1.34	1.25	1.23	26.02	0.04	0.04	0.04	0.21
91.2	5625	9541	9499	230870	1.84	1.97	1.98	41.20	0.02	0.01	0.02	0.22
92.0	439	843	828	19563	1.20	1.45	1.44	29.34	0.06	0.05	0.06	0.27
93.0	170	337	373	8470	0.49	0.64	0.72	13.89	0.04	0.04	0.04	0.20
93.7	198	378	395	8998	0.31	0.40	0.43	8.33	0.04	0.02	0.03	0.14

Table 6: Counts and cross sections corresponding to the different channels at given energies after having used the luminosity and radiation corrections from tab. 5.

4.4 Breit-Wigner fits

The cross sections obtained in table 6 follow the Breit-Wigner distribution

$$\sigma(s) = \frac{12\pi\hbar^2 c^2}{M_{Z_0}^2} \frac{\Gamma_e \Gamma_f s}{(s - M_{Z_0})^2 + \left(\frac{s^2 \Gamma_{Z_0}}{M_{Z_0}}\right)^2}$$

where Γ_e is the partial electron width and Γ_f the partial width of the final state. The factor $\hbar c^2$ is inserted to restore SI units, its numerical value is $0.389 \times 10^6\,\mathrm{nb\,GeV^2}$. This distribution was first fitted[5] to the electron cross section. The partial electron width Γ_e obtained here was than used for the the other fits. The Breit-Wigner cross section is visualized in figure 15 for the electrons and in appendix B for the other final states. The results of the fits

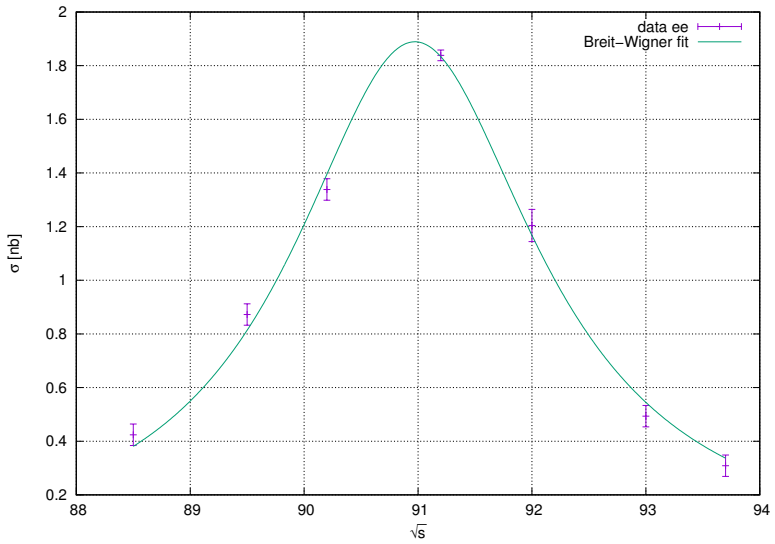

Figure 15: Cross section of the *ee*-channel with corresponding Breit-Wigner distribution.

channel	M_{Z_0} [GeV]	ΔM_{Z_0}	Γ_{channel} [GeV]	$\Delta\Gamma_{\text{channel}}$	Γ_{Z_0} [GeV]	$\Delta\Gamma_{Z_0}$ [GeV]	χ^2_{red}
ee	90.99	0.05	0.09	0.01	2.64	0.31	2.64
$\mu\mu$	91.22	0.01	0.10	0.01	2.71	0.06	0.31
$\tau\tau$	91.21	0.02	0.08	0.01	2.52	0.10	0.60
qq	91.20	0.01	1.75	0.09	2.55	0.06	3.50
total	91.16	0.01	2.02	0.09	2.62	0.04	

Table 7: Mass, partial and total width of the Z^0 from the Breit-Wigner fits.

are shown in table 7. The last line contains the average Z^0-mass and -width as well as the the sum of the partial widths. It was not gained by an additional fit but by usage of the four explained ones. Our result for M_{Z_0} is not in good agreement with the literature value of 91.188 GeV but it is in a 3σ-region and therefore reasonable. It is similar with the total decay width $\Gamma_{Z_0} = 2.495\,\mathrm{GeV}$. In contrast to this the leptonic width (literature value $\Gamma_{ll} = 0.085\,\mathrm{GeV}$) could

[5] All the fits were performed with gnuplot and the errors were directly obtained by the results of the fits.

be confirmed to be universal and it agrees within the errors with the literature. The partial hadronic width agrees with the literature value $\Gamma_{\mathrm{qq}} = 1.727\,\mathrm{GeV}$ as well.

Reasons for the only moderately well behaviour of $M_{\mathrm{Z_0}}$ and $\Gamma_{\mathrm{Z_0}}$ could come from a not optimal choice of the cuts that e.g. classify events like in fig. 14 falsely. An other reason could be that the MONTE-CARLO-simulations do not take the physics of the detector into account perfectly. In addition the radiation corrections are not properly understood by us so we cannot judge whether they are a source of additional uncertainties.

With the results of the four different fits (tab. 7) and the theoretical value of $\Gamma_{\nu\nu} = 0.17\,\mathrm{GeV}$ one can now calculate the number of light neutrinos n_ν.

$$n_\nu = \frac{\Gamma_{\mathrm{Z_0}} - \Gamma_{ee} - \Gamma_{\mu\mu} - \Gamma_{\tau\tau}}{\Gamma_{\nu\nu}} = 3.56 \pm 0.76 \tag{9}$$

This result agrees within the error with the expectation of $n_\nu = 3$. On the other hand it also agrees with $n_\nu = 4$ so that our aim to limit the number of families of elementary particles to three over the number of light neutrinos was not achieved.

4.5 Forward-Backward-Asymmetry

Another interesting property of the Z^0-decay is its forward-backward-asymmetry. It was measured via the $\mu\mu$-channel as it does not have problems with additional terms from t-channel events like $ee \to ee$ and has nearly always two clear tracks in contrast too the tauonic and hadronic final states. This allows to gain the forward-backward-asymmetry simply by counting the number of muon events with $\cos\theta < 0$ and with $\cos\theta > 0$. The forward-backward-asymmetry then is

$$\begin{aligned} A_{\mathrm{fb}} &= \frac{N_+ - N_-}{N_+ + N_-} \\ \Delta A_{\mathrm{fb}} &= \sqrt{\left(\frac{2N_+}{(N_+ + N_-)^2}\right)^2 N_- + \left(\frac{2N_-}{(N_+ + N_-)^2}\right)^2 N_+} \end{aligned}$$

using $N_+ = N(\cos\theta > 0)$ and $N_- = N(\cos\theta < 0)$. Our data can be found in

$\sqrt{s}$ [GeV]	N_-	N_+	A_{fb}	ΔA_{fb}	$A_{\mathrm{fb}}^{\mathrm{theory}}$
88.48	74	49	-0.20	0.09	-0.24
89.47	164	149	-0.05	0.06	-0.14
90.23	327	281	-0.08	0.04	-0.07
91.24	4530	4450	-0.01	0.01	0.02
91.97	390	405	0.02	0.04	0.09
92.97	124	184	0.19	0.06	0.17
93.72	154	199	0.13	0.05	0.23

Table 8: Measured forward-backward-asymmetry compared to the theoretical values.

table 8 where it is directly compared to the theoretical values calculated with given energies and $\sin^2\theta_W = 0.2312$. All the measured values have the same order of magnitude as the literature values and three of the seven values lie within

the σ-interval which is a reasonable result. Comparison with table 2 does not really exclude $\sin^2\theta_W = 0.21$ nor $\sin^2\theta_W = 0.25$ as these deviations are smaller than the statistical errors of the measured forward-backward-asymmetry. On the other hand we can confirm that $\sin^2\theta_W = 0.23 \pm 0.02$ is a reasonable range for the WEINBERG angle.

5 Conclusion

In this experiment we were able to understand the most important ingredients to an analysis of particle decays at a modern detector system. We were able to develop an ensemble of cuts to select events from the different possible final states of the decay of the Z^0. In order to determine physical results from the data we also investigated the efficiency of our selection using MONTE-CARLO-simulations.

With the efficiency-corrected data we were able to determine the mass and width of the Z^0. However the values are only compatible to the literature within an interval of 3σ. Conclusively the values obtained are in a reasonable range of the exact mass.

The partial widths of the four channels we investigated during the experiment could be determined in agreement with the literature. From those values and the theory prediction for the partial width in the neutrino channel we were able to confirm that the number of light neutrinos is compatible with 3.

A measurement of the forward-backward-asymmetry in the $\mu\mu$-decay-channel yields that the data is compatible with a WEINBERG-angle of $\sin^2\theta_W = 0.23$, while it could not completely rule out the values of $\sin^2\theta_W = 0.21$ and $\sin^2\theta_W = 0.25$.

We believe that the results could be improved taking into account a higher amount of statistics.

A Data of the first day

Run	Event	NTRK	SUMP	E_ECAL	E_HCAL
2566	163733	2	50.9	82.6	0
2566	165523	2	91.9	90	0
2566	165548	3	82.5	92.3	0
2566	165576	2	80.9	86.8	0
2566	166436	2	83.1	89.5	0
2566	167987	2	83.8	87.5	0
2566	168389	2	87.4	93.2	0
2566	170045	2	69.3	90.7	0
2566	170379	2	86.1	89.4	0.5
2566	197594	2	90.3	90.6	0
2566	197889	2	92.1	88.5	0.5
2570	28178	3	81.7	91.6	0
2570	28499	2	89.6	92.5	0
2570	28743	2	61.1	89.2	0
2570	28777	3	88.4	89.1	0
2570	88224	2	90.9	90.5	0.3
2570	90060	2	64.6	88.8	0
2570	91274	2	95.6	96.2	0
2571	418921	2	93	90.8	0
2571	420590	2	94.1	89.2	0

Table 9: Exemplary data on the ee-channel

Run	Event	NTRK	SUMP	E_ECAL	E_HCAL
2568	80617	2	90.1	1.6	7
2568	84297	2	93	1.6	8.7
2568	85398	2	96.8	2	0
2568	87693	2	89.1	2.3	8.5
2568	89929	2	90.5	1.5	7.2
2568	91048	2	91.8	1.8	4.3
2568	92681	2	86.3	3.7	3.3
2568	93199	2	99.2	1.3	2.9
2568	95202	2	88.2	1.6	3
2568	99962	2	90.9	1.3	6.7
2568	100566	2	95.6	2.5	6.1
2568	100721	2	75.3	3.1	6.8
2568	102167	2	85.2	5.8	4.4
2568	105720	2	98.6	3.6	5.7
2568	106346	2	86.8	1.9	7.9
2568	107030	2	89	1.9	2
2568	107772	2	108.3	2	8.5
2568	108553	2	92.4	3.6	6.7
2568	110610	2	92	1.9	22.6
2570	29023	2	92.6	3.6	5.7

Table 10: Exemplary data on the $\mu\mu$-channel

Run	Event	NTRK	SUMP	E_ECAL	E_HCAL
2566	170371	5	74	51.1	10.2
2566	170508	2	46.5	17.3	8.2
2566	179750	2	30.8	1.6	6.3
2566	184010	2	29.5	10.2	4.1
2566	184435	2	33.1	1.5	10.6
2566	189056	2	24.4	12.4	11.7
2566	208314	4	36	16.1	5.7
2566	212745	2	41.3	11.1	20
2570	29664	2	49.7	5.2	20.3
2570	30348	2	33.4	23.6	6.9
2570	34612	2	14.1	3.3	6.3
2570	39992	2	19.7	15.9	3.8
2570	42200	2	26.8	16.5	3.4
2570	45609	5	23.4	27	17.1
2570	47033	2	23.8	29.4	3.6
2572	98915	2	39	18.9	4.4
2572	102412	2	24.1	46.5	7.3
2572	102586	5	38.5	28.5	0
2572	108411	2	35.3	51.8	2.3
2572	109621	2	17.8	2.5	5

Table 11: Exemplary data on the $\tau\tau$-channel

Run	Event	NTRK	SUMP	E_ECAL	E_HCAL
2566	164184	15	37.7	37	14.1
2566	195995	17	39.2	66.8	9.9
2566	196117	46	64.6	53	13
2566	196548	8	33.3	67.5	13.3
2568	78191	36	45.3	53.2	7.7
2568	78425	41	59.9	53.2	13.8
2568	78553	9	21.9	65.2	8.8
2568	78787	16	55.9	50.4	24.3
2568	79038	30	38.1	68.3	13.8
2568	79043	22	34.4	75.5	6.2
2568	79181	36	51.2	62.3	5.5
2568	79337	23	63.1	56	17.2
2568	79487	23	59	60.6	8.5
2568	79517	26	62.2	67.2	20.4
2568	79642	30	43.3	71.7	4.3
2570	88252	40	47.8	61.4	5.7
2570	88262	19	67.9	52.1	10.6
2570	88303	14	52.1	61	4.4
2570	88328	29	82.6	53.8	16.4

Table 12: Exemplary data on the $q\bar{q}$-channel

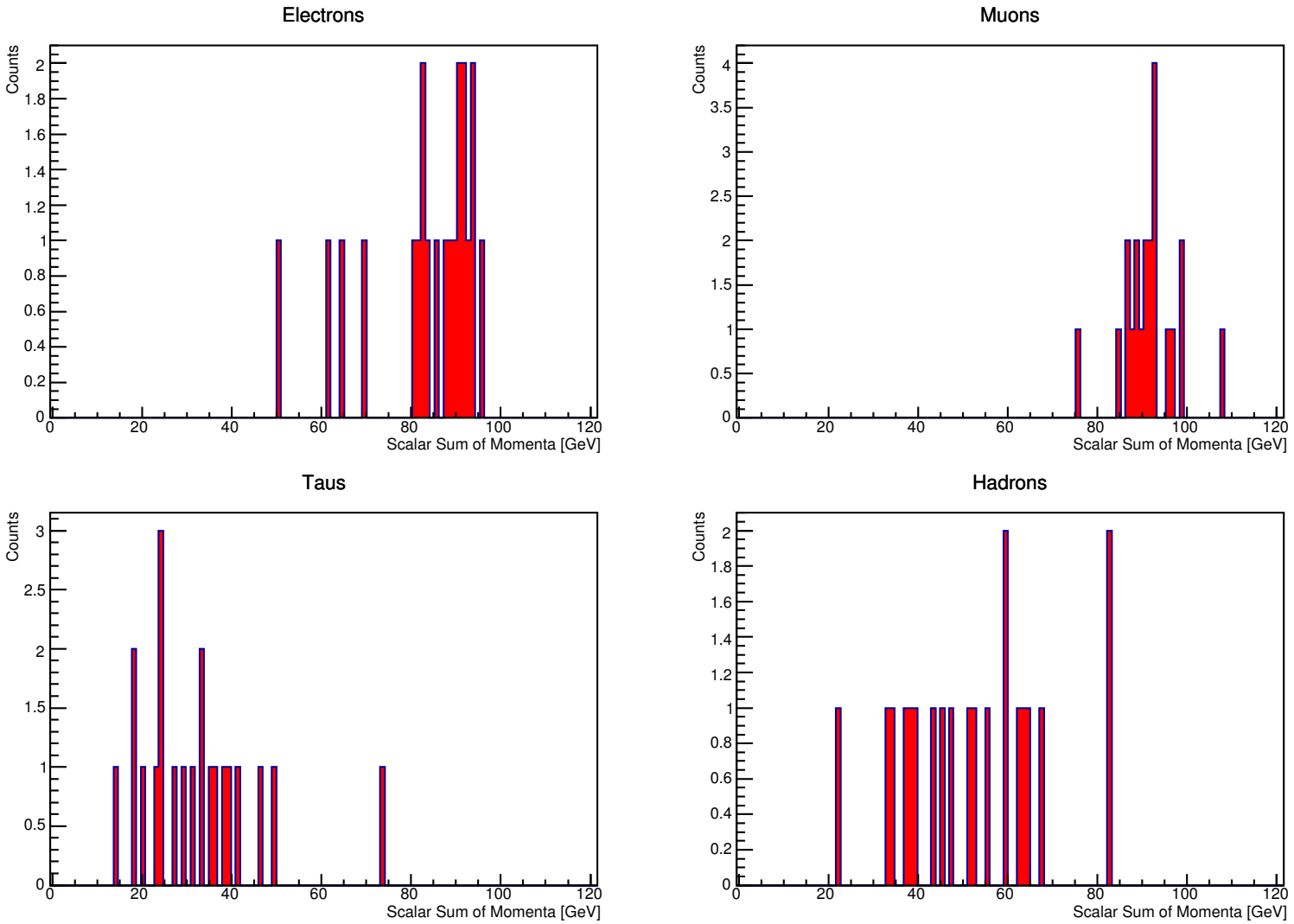

Figure 16: Histogram of the scalar sum of the momenta for the different channels

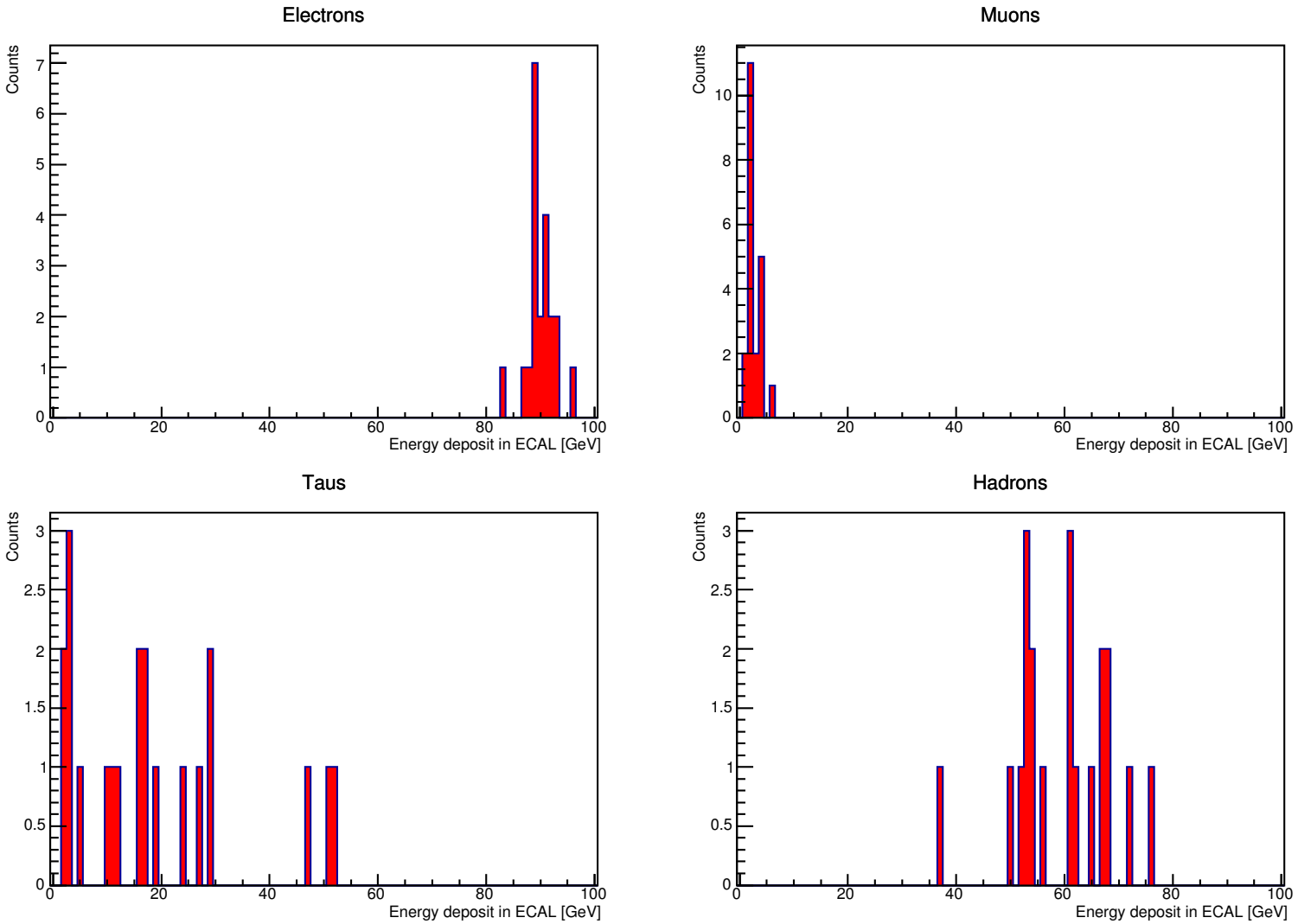

Figure 17: Histogram of the energy deposit in the electromagnetic calorimeter for the different channels

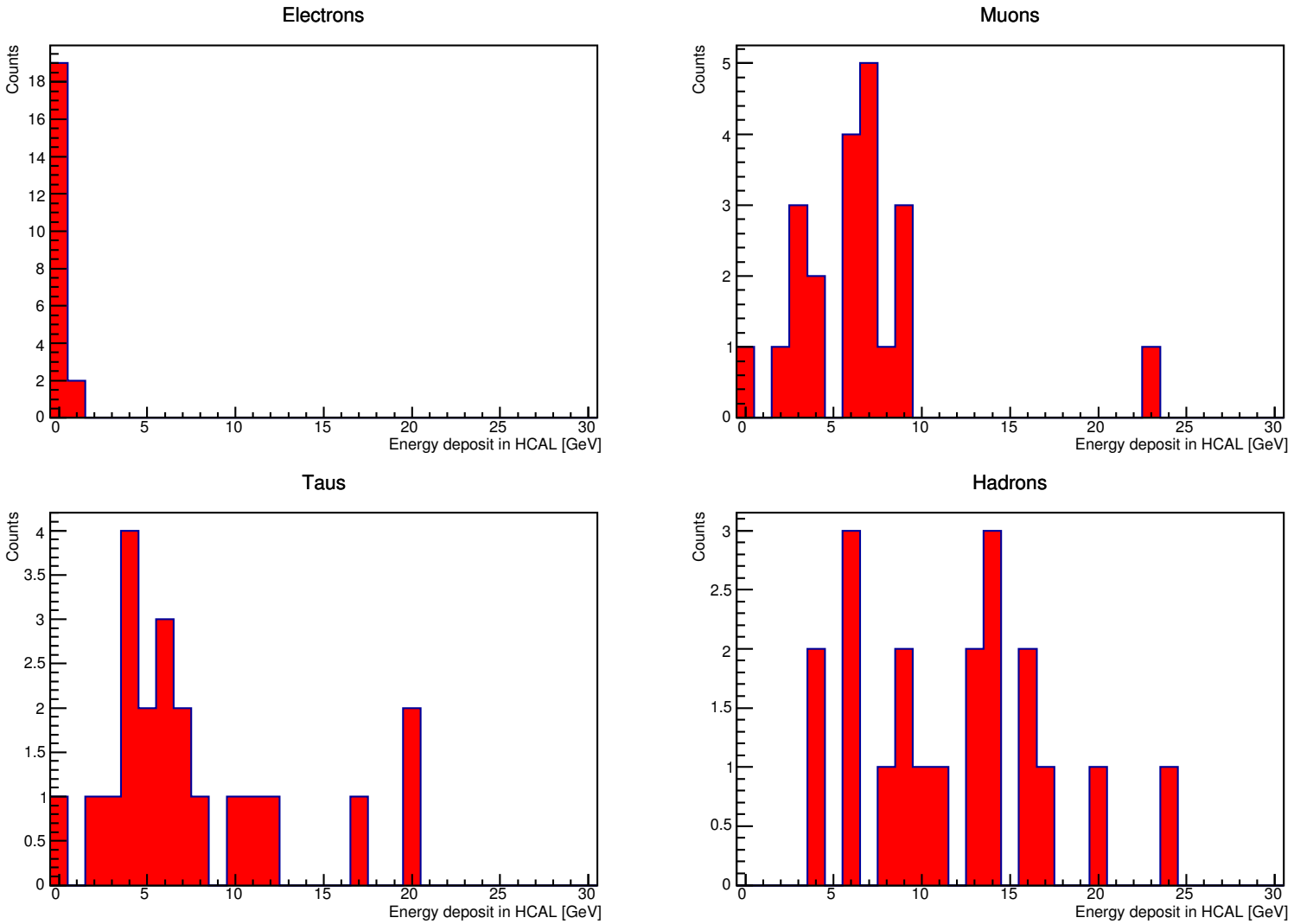

Figure 18: Histogram of the energy deposit in the hadronic calorimeter for the different channels

B Breit-Wigner fits of muons, tauons, and hadrons

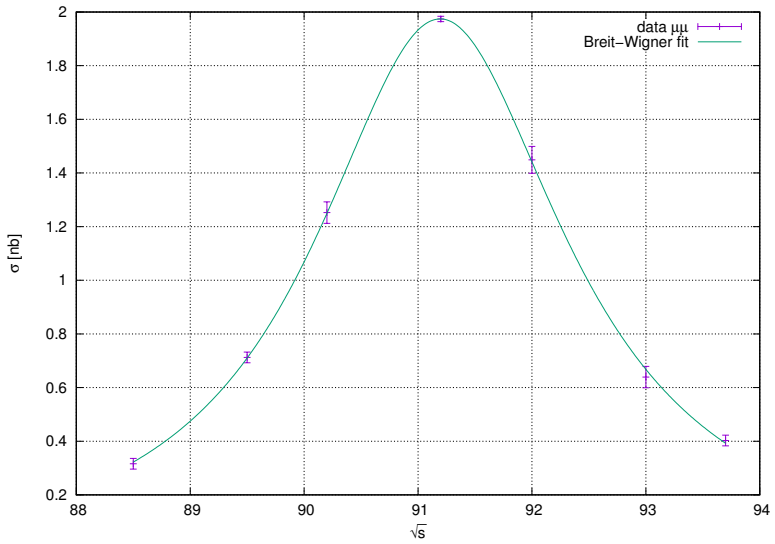

Figure 19: Cross section of the $\mu\mu$-channel with corresponding Breit-Wigner distribution.

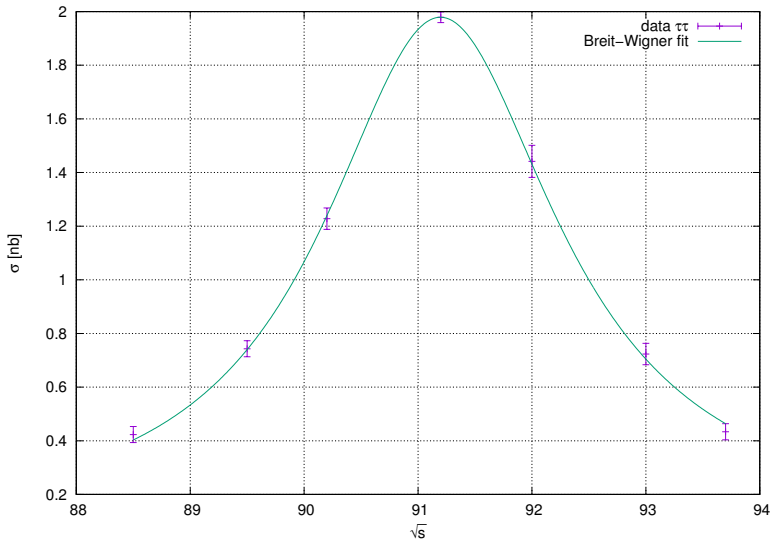

Figure 20: Cross section of the $\tau\tau$-channel with corresponding Breit-Wigner distribution.

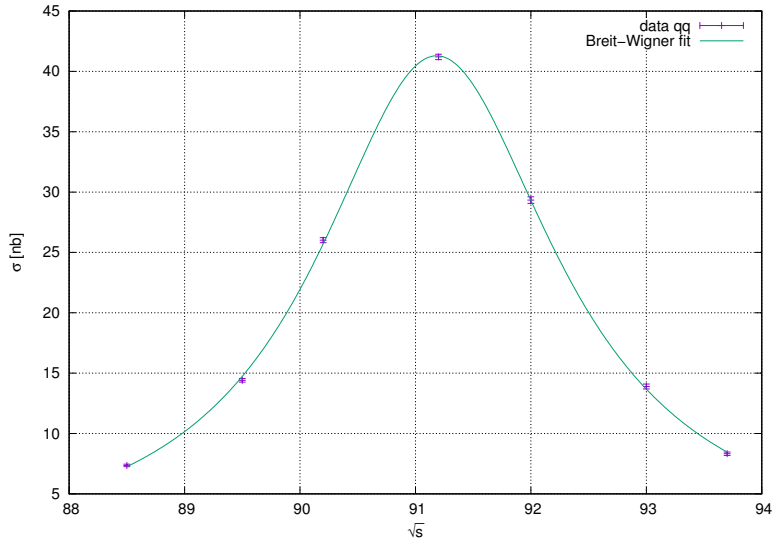

Figure 21: Cross section of the qq-channel with corresponding Breit-Wigner distribution.

List of Figures

List of Tables

References

[E213] Advanced Physics Laboratory Course Part II: Instructions for E213 Analysis of Z^0 decays

[UCL] `http://www.hep.ucl.ac.uk/~jpc/all/ulthesis/node16.html` - Last accessed on 4th of June

[WiBW] `https://de.wikipedia.org/wiki/Breit-Wigner-Form` - Last accessed on 10th of June

[PDG-Z] `http://pdg.lbl.gov/2012/listings/rpp2012-list-z-boson.pdf` -Last accessed on 10th of June

[FGst] `https://i.stack.imgur.com/Xoibk.png` - Last accessed on 10th of June